IEEE Access
Multidisciplinary | Rapid Review | Open Access Journal

Received 28 May 2023, accepted 23 June 2023, date of publication 30 June 2023, date of current version 18 July 2023.

Digital Object Identifier 10.1109/ACCESS.2023.3291339

RESEARCH ARTICLE

A Modified PWM Strategy With an Improved ANN Based MPPT Algorithm for Solar PV Fed NPC Inverter Driven Induction Motor Drives

NAZMUL ISLAM NAHIN[1], SHUVRA PROKASH BISWAS[1], (Student Member, IEEE), SUDIPTO MONDAL[1], MD. RABIUL ISLAM[2], (Senior Member, IEEE), AND S. M. MUYEEN[3], (Senior Member, IEEE)

[1]Department of Electronics and Telecommunication Engineering, Rajshahi University of Engineering and Technology, Rajshahi 6204, Bangladesh
[2]School of Electrical, Computer and Telecommunications Engineering, University of Wollongong, Wollongong, NSW 2522, Australia
[3]Department of Electrical Engineering, Qatar University, Doha, Qatar

Corresponding author: S. M. Muyeen (sm.muyeen@qu.edu.qa)

Open Access funding provided by the Qatar National Library.

ABSTRACT The integration of solar photovoltaic (PV) arrays for induction motor drives (IMDs) has attained a lot of research interest due to the versatile applications of IMD including water pumping, cement industries, electric vehicles, and rolling mills etc. Multilevel inverters (MLIs) are a prominent solution for driving medium voltage induction motors (IMs) due to their superior performances over two-level voltage source inverters (VSIs). However, the power quality performance of MLI fed IMDs greatly depends on the pulse width modulation (PWM) strategy employed. Traditional PWM strategies for MLIs suffer from power quality problem such as lower order harmonics, high THD, unbalanced power loss distribution, high switching power loss, thermal instability and electromagnetic interference (EMI) problems. In this paper, a modified PWM strategy is proposed for a solar PV fed 3-level neutral point clamped (NPC) inverter driven IMD. The proposed PWM strategy introduces a new modulating signal with level shifted triangular carriers. The proposed modulating signal is formed by utilizing a 13^{th} harmonic signal and saturated balanced 3-phase sinusoidal signals. The proposed PWM technique is named as 13^{th} harmonic injected 60°-PWM (THISDPWM). The THISDPWM reduces the lower order harmonics contents, overall THD, and switching power losses of the NPC inverter compared to different existing PWM strategies. Apart from that, a robust artificial neutral network (ANN) based incremental conductance maximum power point tracking (MPPT) algorithm is also introduced to control the dc-link voltage of the PV fed NPC inverter driven IMD system. The presented ANN based dc-link controlled technique ensures stable dc-link voltage against wide range of PV parameters variation. All the simulation works are carried out in MATLAB/Simulink environment and a reduced scale laboratory prototype of the IMD is built and tested to validate the performance of the proposed THISDPWM technique.

INDEX TERMS Pulse width modulation, neutral point clamped inverter, solar photovoltaic, artificial neural network, induction motor drive, power quality, total harmonic distortion.

I. INTRODUCTION

The recent depletion of non-renewable energy resources is influencing the globe to choose an alternative to meet the enormous energy demands. The need for renewable energy sources is growing as everyday consumption of conventional energy sources decreases. Solar energy sources are viable renewable sources due to their accessibility, cost-effectiveness, and environmental friendliness. Although dc motors have been used with photovoltaic (PV) arrays for many years, induction motor (IM) have replaced them because of their durability, reliability, and

The associate editor coordinating the review of this manuscript and approving it for publication was Feifei Bu.

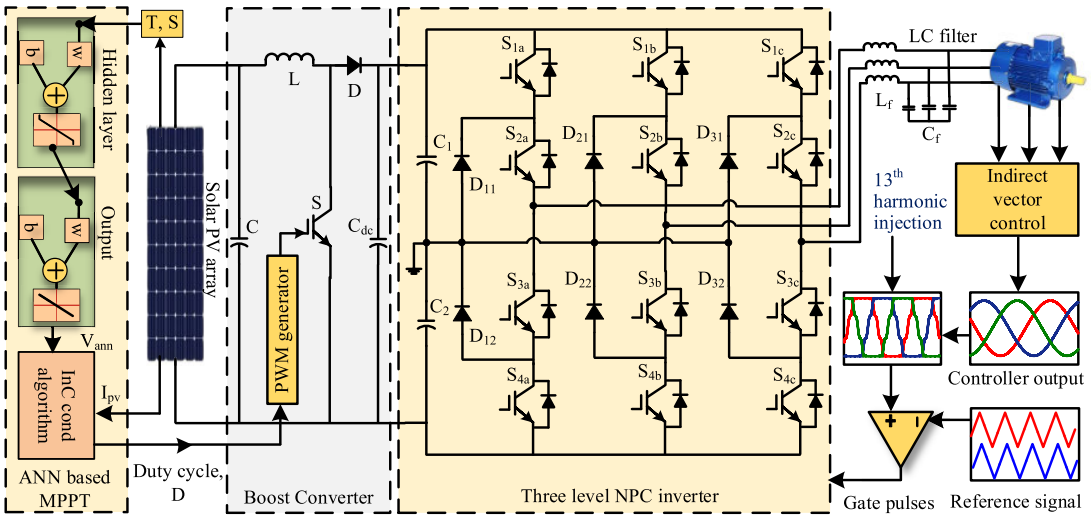

FIGURE 1. Structure of the PV fed NPC inverter driven IMD.

ease of maintenance [1]. The integration of solar PV arrays with the induction motor drives (IMDs) has been a field of interest among researchers. Solar insolation and temperature are the key parameters of solar PV arrays to extract the maximum power from them and maintain the system's reliability.

Several maximum power point tracking (MPPT) algorithms have been investigated including perturb & observe (P&O), incremental conductance (InC), and hill climb (HC) algorithms, which vary from each other in terms of tracking capability and effectiveness [2], [3], [4]. In [5], an innovative P&O scheme for MPPT of a PV system built on linear tangents has proposed. A novel method to track the global maximum power point (GMPP) under partially shaded conditions have discussed in [4]. In [6], a hybrid approach has taken for maximum power point monitoring for PV applications using hill climbing (HC) techniques to enhance the performance of PV system at different insolation conditions. The main limitation of traditional MPPT methods is their inability to effectively control or suppress the oscillations of the operating point of PV system around its MPP. This oscillatory behavior can cause power losses in the PV system during steady-state operation, and can also result in inaccurate MPP tracking in shaded conditions.

On the contrary, artificial intelligence (AI) based MPPT has gained much popularity due to its tracking capability, fast speed of convergence, and reduced transient state [7], [8], [9]. An advanced genetic algorithm (GA) based proportional integral derivative (PID) controller with variable step size MPPT is presented in [10] which is very complex and requires high computational power. In [11], a fuzzy logic based MPPT controller for a PV system has investigated thoroughly. But the fuzzy MPP controller mainly depends on the user's knowledge and experience of having applied fuzzy in a PV system and selecting a membership function. A constant voltage based MPPT for photovoltaic applications to enhance the performance using genetic algorithm is examined in [12]. The problem of using GA is the ability to enforce inequality constraints, as well as sensitivity to the initial population and a decrease in solution quality as the problem size grows larger.

To mitigate the short comings of above mentioned traditional MPPT techniques and AI based dc-link controllers, the development of a robust AI based dc-link controller is always an industrial demand. In this work, an ANN based MPPT technique is also proposed to improve the performance of the dc-link dynamics of the PV fed IMD system. The proposed ANN based MPPT technique is based on incremental conductance (InC) algorithm.

Apart from PV side, the power quality parameters of IMD system largely depend on the motor driving inverter. For driving induction motor in a PV integrated IMD system, multilevel inverters (MLIs) have replaced conventional two-level inverter due to their superior performances such as low dv/dt stress, low total harmonic distortion (THD), improved power quality, modularity, and reduced common mode voltage [13]. The most common and traditional multilevel inverter (MLI) topologies are neutral-point-clamped (NPC) MLI, cascaded H-bridge (CHB) MLI, and flying capacitor (FC) MLI. CHB-MLI got the upper hand among the topologies regarding the voltage balancing issue [14], [15]. However, it requires separate isolated dc sources, making the converter bulky and costly. In the case of FC-MLI, a complex algorithm is required to properly to regulate the flying capacitor and dc-link voltages properly, as the level increases, complexity rises [16]. On the contrary, NPC-MLI manages the fundamental output phase voltage while simultaneously reducing the amount of the THD that results in losses and pulsating torque in medium power drives. It is extensively used in the industry due to its increased medium voltage management capabilities, high power density, and ease of maintenance [17]. Therefore, this work utilizes a three-level NPC inverter to drive the IM.

However, the power quality and losses of an NPC inverter is greatly influenced by the pulse width modulation (PWM) employed. Numerous PWM methods have been mentioned in the literature [18], [19], [20] for improving the power quality and loss of NPC inverter, including sinusoidal PWM (SPWM), conventional space vector PWM (CSVPWM), and third harmonic injected PWM (THPWM) to reduce the harmonics generated by solar PV fed inverter [21]. Moreover, hybrid PWM approaches such as trapezoidal PWM (TRPWM), third harmonic sixty-degree PWM (THSD-PWM), and sixty-degree bus clamping PWM (SDBCPWM) perform better in reducing switching losses and enhancing IMD performance [22], [23]. Regarding torque ripple, the TRPWM outperforms than other techniques [24]. On the other hand, the CSVPWM, TRPWM, and SDBCPWM exhibit improved dc-link voltage utilization and dynamic performance of the IMD. The CSVPWM has considered the touchstone for PWM techniques as the method offers 15% more fundamental voltage than the SPWM technique while keeping the dc-link voltage constant [25]. However, as the level of MLI increases, the CSVPWM increases in complexity and requires huge computation. In [26], SDPWM based on multiple odd harmonics injection has presented. But this method suffers from increased harmonics at the inverter end. An adaptive THPWM method is proposed in [27], to reduce harmonics. Moreover, these techniques cannot reduce harmonics and switching losses to the extinct of degrading the quality of motor end parameters such as torque ripple, speed, and stator currents.

To mitigate the shortcomings of above mentioned PWM technique and for further improvement of the performance NPC inverter driven IMD, a modified PWM technique is proposed based on the 13th harmonics injection technique with the modulating signal of 60°-degree PWM which is named as 13th harmonic injected 60°-PWM (THISDPWM). The proposed THISDPWM technique improves the THD of the inverter as well as the stator voltage/current of the IM, total power loss, and torque ripple of the IM. The main contributions of this paper are summarized as follows:

- A robust ANN based MPPT technique for controlling the dc-link of the system;
- A modified PWM technique is proposed for the NPC inverter;
- THD reduction of the motor voltage and current;
- Reduction of total power loss; and
- Reduced torque ripple of the motor.

II. SYSTEM DESCRIPTION

The system structure of the IMD is depicted in Fig. 1. The presented system consists of a 20kW PV array for driving a 3-phase, 15.5kW, 400V, 50Hz induction motor depicted. The PV voltage is boosted up by the dc-dc boost converter. The output of the dc-dc boost converter is fed to the input of the NPC inverter. An ANN based InC MPPT technique is utilized to extract the maximum power from the PV array which develops the dc-link voltage for the inverter. A second-order LC filter is employed at the inverter end to suppress the unwanted harmonics from the supply.

TABLE 1. Parameter values for training the model.

Parameter	Value
Maximum irradiance, IR_{max}	1000W/m^2
Minimum irradiance, IR_{min}	0 W/m^2
Maximum temperatue, $Temp_{max}$	45°C
Minimum, $Temp_{min}$	10°C
Voltage at MPP, V_{MP}	29V
Temperature coefficient of V_{oc}, β	-0.36099 V/°C
Standard temperature, T_s	25°C

A. ESTIMATION OF DC-LINK VOLTAGE

The dc link voltage for the NPC inverter is calculated as [28],

$$V_{dc} = \frac{2\sqrt{2}}{\sqrt{3}M_i} V_{L-L} \tag{1}$$

$$V_{dc} = 1.613 \times 400 \cong 650V \tag{2}$$

where, V_{L-L} is the line-to-line voltage which is taken as 400V. and M_i represents the modulation index which is taken as 1 for calculation.

B. PROPOSED ANN BASED INCREMENTAL CONDUCTANCE MPPT ALGORITHM

Fig. 2 shows the ANN based MPPT system with two inputs, three neurons and one output. The structure that is utilized in this model is feedforward multilayer neural network. The solar irradiance, IR and temperature, T are used as the inputs to the system. The maximum generated voltage, V_{MPP} is considered as the output of the system. To obtain the training dataset based on these parameters the following equations are utilized,

$$IR = [(IR_{\max} - IR_{\min}) \times rand] + IR_{\min} \tag{3}$$

$$Temp = [(Temp_{\max} - Temp_{\min}) \times rand] + Temp_{\min} \tag{4}$$

$$V_{MPP} = V_{MP} + \beta \times (Temp - T_s) \tag{5}$$

where, IR_{max}, IR_{min}, $Temp_{max}$, and $Temp_{min}$ are the maximum and minimum irradiance and temperature of the solar panel, respectively and V_{MP}, β and T_s represents the maximum voltage at MPP, voltage temperature co-efficient, and standard temperature, correspondingly.

The parameter values for which the dataset is obtained is shown in Table 1.

These parameters are selected by the neural network and modified them by weights and biases before sending to the neurons in the subsequent layer. The neuron of each layer of the neural network gets information from previous layer. The model forecasts the corresponding maximum power voltage and current values by using the operating temperature and radiation of the PV array as input values. Each input signal

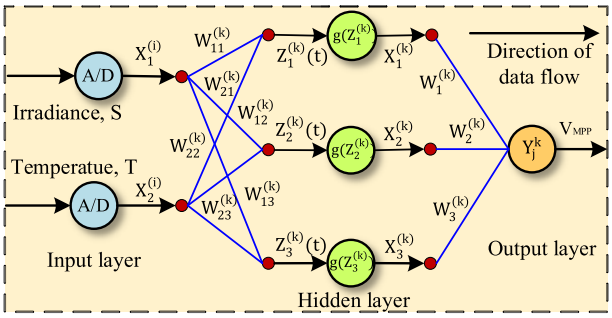

FIGURE 2. Structure of the feed forward neural network.

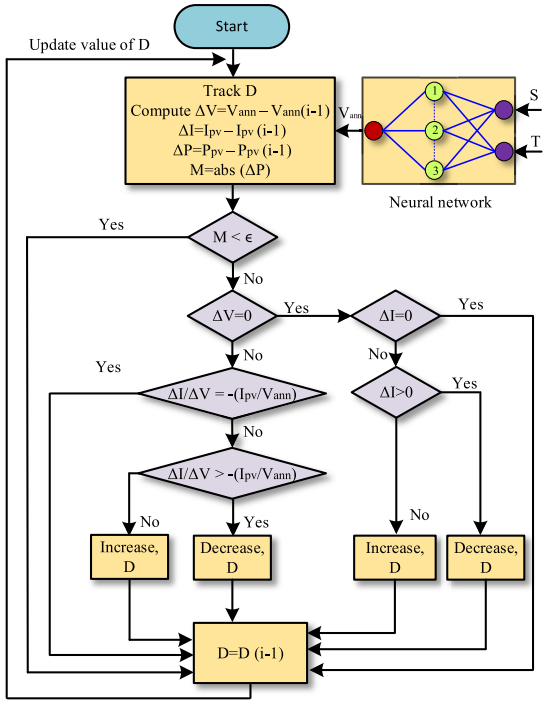

FIGURE 3. Flowchart of the proposed ANN based MPPT algorithm.

is added together after being multiplied by the weights of the hidden layer to create the output neuron which is found as,

$$y_j^k = f\left(\sum_{i-1}^{N} W_{ji}X_i + b_j\right) \tag{6}$$

where, f is the activation function, W_{ij} is the connection weight, X_i is the input and b_j is the deviation value, respectively. The difference between the required output value and the obtained output value can be given as,

$$Error = \frac{1}{2}\sum_{i-1}^{N}\left(y_{jd} - y_j^k\right)^2 \tag{7}$$

where, y_{jd} is the desired output value. MATLAB/Simulink environment were used to get the required data for the training purpose of ANN. To train the neural network, 10000 datasets for irradiance (IR), temperature(T), and generated voltage (V_{MPP}) of the selected solar panel are used. If the ANN is subjected to a novel input, it will generalize to new scenarios by analyzing the relationship between the input and output similar to the training data. With 70% going to the training set and 15% going to each of the validation and testing sets, the entered data were divided into three categories at random. Levenberg-Marquardt (LM) algorithm were used for the training purpose. The number of hidden layers were obtained based on the satisfactory performance of the model. To verify the performance and accuracy of the neural network, two performance indices named mean squared error (MSE) and correlation coefficient (R) are considered which are given as in [26],

$$MSE = \frac{1}{N}\sum_{i=1}^{N}\left(\hat{V}_{est} - V_{MPP}\right)^2 \tag{8}$$

$$R = \sqrt{1 - \frac{\sum_{i=1}^{N}\left(\hat{V}_{est} - V_{MPP}\right)^2}{\sum_{i=1}^{N}(V_M)^2}} \tag{9}$$

where, N is the sampling size, $\hat{V}_{est}$, V_{MPP}, and V_M represents the estimated value generated from the neural network, actual voltage at MPP and measured value, respectively.

The obtained voltage, V_{MPP} is then fed to the incremental conductance algorithm along with the current, I_{pv} to determine the duty ratio, D for the dc-dc boost converter. Fig. 3 depicts the flowchart of the incremental conductance used in conjunction with the ANN based MPPT technique. This algorithm first determines the power, P and then calculates the changes in voltage, ΔV, power, ΔP, and the current, ΔI from their previous values. After that, it calculates the incremental power change, M as the absolute value of the power change, ΔP. The function returns the prior duty cycle if the incremental power change, M is less than a predetermined threshold number. Otherwise, it determines whether to slightly increase or reduce the duty cycle, D and then returns the new duty cycle using the sign of the current change, ΔI and the voltage change, ΔV, respectively.

C. MOTOR CONTROL STRATEGY

The basic block diagram of an indirect vector control (IVC) scheme for a 3-level NPC inverter fed IMD is depicted in Fig. 4. In this system, the stator d-axis current, i_{sd} and q-axis current, i_{sq} control the flux and torque independently. The reference torque, $T_e{}^*$ is used to estimate the reference q-axis current, $i_{sq}{}^*$ as,

$$i_{sq}^* = K_t T_e^* \tag{10}$$

where, $K_t = \frac{4L_r}{3PL_m\psi_{est}}$, L_r is the inductance of the rotor, P is the number of poles of the motor, L_m is the mutual inductance and ψ_{est} is the estimated rotor flux of the induction motor, respectively.

The rotor reference flux, ψ_r^* is used to calculate the reference stator d-axis current, $i_{sd}{}^*$ which is given as,

$$i_{sd}^* = \frac{\psi_r^*}{L_m} \tag{11}$$

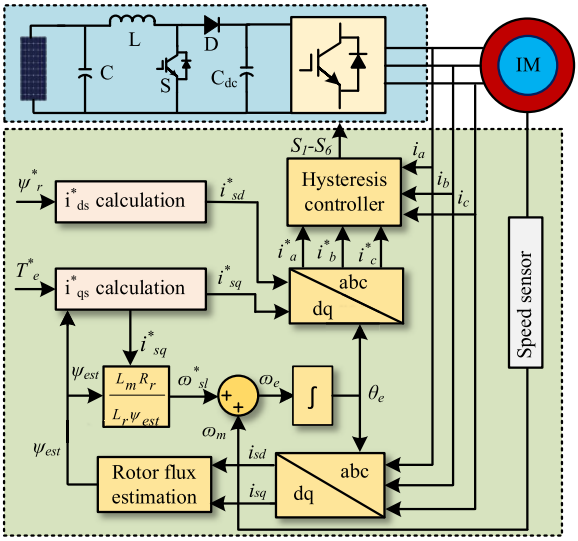

FIGURE 4. Motor control strategy based on indirect vector control.

The slip speed, ω_{sl}^* is used to determine the rotor angle, θ_e which is needed for co-ordinate transformation,

$$\omega_{sl}^* = \frac{L_m}{\psi_{est}} \cdot \frac{R_r}{L_r} \cdot i_{sq}^* \tag{12}$$

The rotor angle, θ_e is then calculated as,

$$\theta_e = \int \omega_e dt = \int (\omega_m + \omega_{sl})\, dt = \theta_m + \theta_{sl} \tag{13}$$

The reference q-axis and d-axis currents, $i_{sq}{}^*$ and $i_{sd}{}^*$ are fed to dq transformation block to obtain the reference 3-phase stator currents ($i_a{}^*$, $i_b{}^*$, and $i_c{}^*$) which are subtracted from the actual stator currents (i_a, i_b, i_c) to find the current error. The error is processed by the hysteresis controller and generate the necessary gate pulses for the 3-level NPC inverter.

III. TRADITIONAL AND PROPOSED PWM STRATEGIES

In this section different existing PWMs techniques has been shown. After that the detail description about the proposed PWM strategy is described.

A. TRADITIONAL PWM STRATEGIES

The frequently used PWM methods for MLIs are SPWM, THSDPWM, CSVPWM, SDPWM, and THPWM [18], [20]. These PWM techniques are based on the injection of different common mode signal with balanced 3-phase sinusoidal signals incoming from the controller. THPWM is popular for reducing lower order harmonics from inverter output voltage as compared to SPWM.

On the contrary, CSVPWM has better dc-bus utilization capability than other existing PWM methods. However, compared to the SPWM, CSVPWM, and THPWM, the SDPWM and THSDPWM have higher harmonic suppression capabilities due to the flattened top surface on their modulating signal [22]. The modulation signals correspond to SPWM, THSDPWM, CSVPWM, SDPWM, and THPWM methods, respectively. Ra, Rb, and Rc of Fig. 5 represent the three balanced modulating signals which are separated by 0°, -120°, and 120°, respectively.

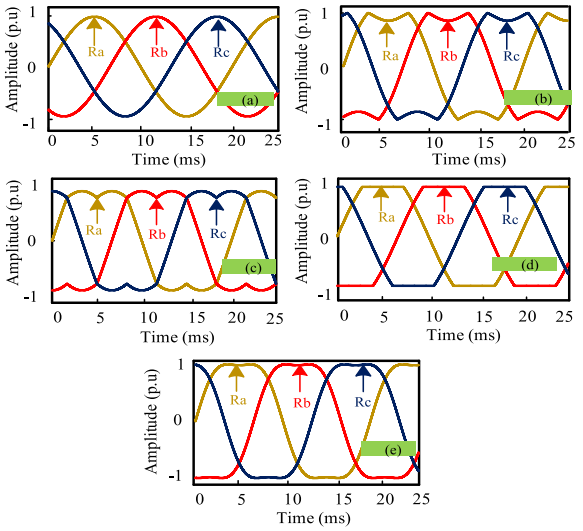

FIGURE 5. Reference modulation signals with the switching strategy: (a) SPWM [11], (b)THSDPWM [12], (c) CSVPWM [16], (d)SDPWM [17], and (e) THPWM [18].

B. PROPOSED PWM STRATEGY

The proposed PWM strategy is developed based on 13th harmonic injection with 60° clamped intermediate signal which is named as 13th harmonic injected 60°-PWM (THISDPWM). The step-by-step algorithm for developing the modulation signal of the THISDPWM strategy is presented in Fig. 6. The output of the controller which is a fundamental three phase sinusoidal signals are represented by Z_1, Z_2, and Z_3 which can be expressed as,

$$Z_1 = B_m \sin\left(\omega t + 0°\right) \tag{14}$$
$$Z_2 = B_m \sin\left(\omega t - 120°\right) \tag{15}$$
$$Z_3 = B_m \sin\left(\omega t + 120°\right) \tag{16}$$

where, $B_m \in$ [-1.5, 1.5]. After applying saturation operation to the signals (14)-(15), The amplitude is kept between -p to p. Thus, the 60° clamped intermediate signal is obtained, which can be expressed as,

$$Z_4 = qB_m \sin(\omega t + \theta) \tag{17}$$

where, q ∈ [-1, 1] and $\theta = 0°$, -120°, and 120°.

A 13th harmonic sinusoidal signal is represented by K and can be written as,

$$Z_5 = rA_m \sin(13\omega t + \theta) \tag{18}$$

where, r represents the peak amplitude of Z_5 and $r = 0.01$.

Now, the summation of these the two signals, K and W is expressed as,

$$\begin{aligned} Z_6 &= Z_4 + Z_5 \\ &= qB_m \sin(\omega t + \theta) + rA_m \sin(13\omega t + \theta) \end{aligned} \tag{19}$$

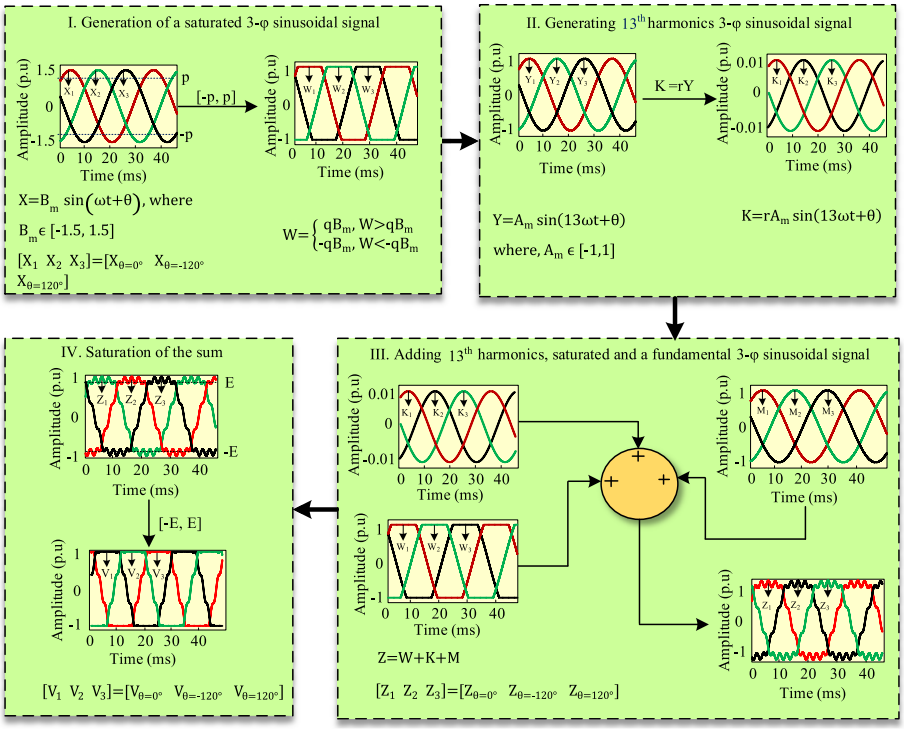

FIGURE 6. Step by step development of the modulation signal of THISDPWM strategy.

TABLE 2. Switching states of 3L-NPC inverter.

Status of switches					
S_{1x}	S_{2x}	S_{3x}	S_{4x}	Switching state	Output voltage
1	1	0	0	[P]	$V_{dc}/2$
0	1	1	0	[O]	0
0	0	1	1	[N]	$-V_{dc}/2$

Now, a fundamental sinusoidal signal of magnitude one is added with signal Z_6 which is indicated as, V and can be expressed as,

$$V = qB_m \sin(\omega t + \theta) + rA_m \sin(13\omega t + \theta) + C \sin(\omega t + \theta) \quad (20)$$

where, C ∈ [-1, 1] and $\theta = 0°$, -120°, and 120°.

Applying saturation operation within limit [-E, E], the final proposed modulation signal of THISDPWM strategy is obtained which can be expressed as,

$$\left[V_1 \; V_2 \; V_3 \right] = \left[V_{\theta=0°} \; V_{\theta=-120°} \; V_{\theta=120°} \right] \quad (21)$$

The proposed modulation signal is then compared with high frequency level shifted triangular carrier signals to generate the gate pulses for the IGBTs of the 3-phase NPC inverter.

C. OPERATING PRINCIPLE AND ANALYSIS OF THE PROPOSED THISDPWM SCHEME

The three-level NPC inverter topology shown in Fig. 1 operates on three switching states presented in Table 2. The modulation signal and corresponding gate pulses generation using THISDPWM scheme for leg-1 is illustrated in Fig. 7.

In R-II and R-IV, the modulation signal is clamped to +1([P] state) and -1 ([N] state), respectively.

In R-I, switching state changes between [P] and [O], when the modulation signal is positive and switching state changes between [N] and [O], when the modulation signal is negative which can be seen in R-III and R-V.

From Fig. 7, it can be seen that, the proposed THISDPWM scheme produces flatted top surface which leads to zero switching actions within regions R-II and R-IV, respectively. This feature of the proposed modulating signal aids to reduce the switching loss of the inverter as compared to other existing PWM schemes. On the contrary, due to the symmetricity of the modulating wave while taking in a comparison with high frequency carrier wave as depicted in Fig. 7, the inverter generates balanced and symmetric gate pulses, leading to a low total harmonic distortion (THD) in the output voltage. Thus, the key features of the proposed THISDPWM techniques can be summarized as,

- Flatted top equal loading modulating signal enables the generation of balanced and symmetric gate pulses.
- The balanced and symmetric gate pulses result in low total harmonic distortion (THD)

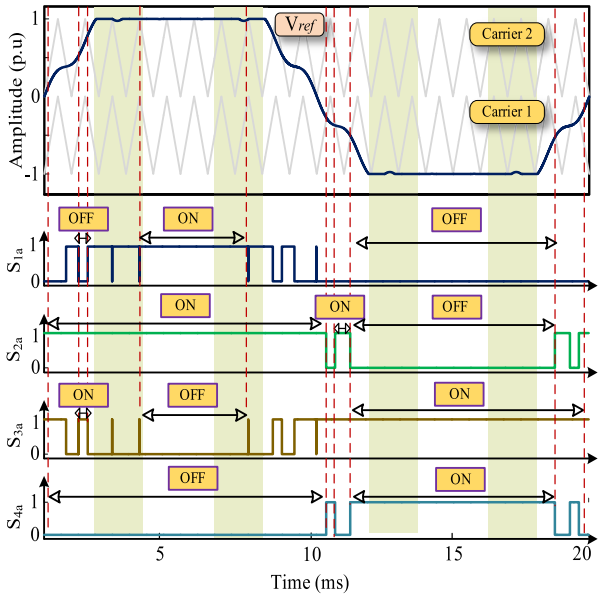

FIGURE 7. Gate pulse generation using THISDPWM technique for a single leg of the 3-level NPC inverter.

- The flatted top modulating signal eliminates the need for switching the IGBTs in R-II and R-IV regions, thereby reducing switching loss in the inverter.

The mathematical expressions of the existing and proposed PWM schemes are presented in Table 3. Most PWM signals are created from the fundamental three sinusoids, which are represented in Table 3 by X_{a1}, X_{b1}, and X_{c1}. The THPWM signal is produced by combining the SPWM signal with a third-harmonic signal. The primary approach for creating new modulation signals is using these signals as multiplier and common mode injection.

IV. PERFORMANCE ANALYSIS OF THE SYSTEM

In this section, various performances of the IMD system including THD analysis of inverter output voltage, dynamic response of the IMD, PV side dynamic response and power loss of the inverter are inspected for different existing and the proposed PWM strategies based on MATLAB/Simulink simulation.

A. THD ANALYIS OF THE INVERTER OUTPUT VOLTAGE

In this sub-section, the output voltage quality of the NPC inverter for different PWM strategies is analyzed at unfiltered condition. The unfiltered inverter output line-to-line voltage is shown in Fig. 8(a) for the proposed THISDPWM strategy. The frequency spectrum of the inverter line-to-line voltage waveform is shown in Fig. 8(b). From Fig. 8(b), it is obvious that the detrimental lower order harmonics are suppressed which ensures good motor health. The THD of the inverter line-to-line voltage is recorded 21.94%. Due to the elimination of lower order harmonics content, the proposed THISDPWM strategy imposes less burden on the filter circuit. A comparative analysis is conducted in Table 4 among different existing PWM strategies and the proposed PWM strategy in terms of inverter line-to-line voltage THD. Table 4 is prepared by varying the modulation index of the PWM techniques. The switching frequency of the inverter was set to 5kHz while preparing Table 4. The THDs are recorded for three different regions which are under, unity, and over modulation region, respectively.

From Table 4, it can be seen that SPWM, THSDPWM, CSVPWM, SDPWM, and THPWM show 44.43, 43.65, 42.39, 43.36, and 41.38% inverter line-to-line voltage THD, respectively at under modulation region ($M_i = 0.7$). Similarly, 35.46, 30.94, 27.58, 28.69 and 26.61% inverter line-to-line voltage THDs are recorded for SPWM, THSDPWM, and THPWM strategies at unity modulation index ($M_i = 1$).

In over modulation region ($M_i = 1.1$), 32.06, 26.67, 25.91, 25.99 and 24.76% inverter line-to-line voltage THDs

TABLE 3. Mathematical representation of the traditional and existing PWM schemes.

PWM scheme	Mathematical Expression
SPWM [17]	$X_1 = A\sin(\omega t+\theta)$ $[X_{1a} \quad X_{1b} \quad X_{1c}] = [X_{\theta=0^\circ} \quad X_{\theta=-120^\circ} \quad X_{\theta=120^\circ}]$
THPWM [24]	$B = kA\sin(3\omega t+\theta)$ $X_2 = A\sin(\omega t+\theta)+B$ $[X_{2a} \quad X_{2b} \quad X_{2c}] = [X_{\theta=0^\circ} \quad X_{\theta=-120^\circ} \quad X_{\theta=120^\circ}]$
THSDPWM [18]	$S_1 = X_1$ $= 0.76A\,(when\ X_1 > 0.76A)$ $== -0.76A\,(when\ X_1 < -0.76A)$ $X_3 = S_1 = B$ $[X_{3a} \quad X_{3b} \quad X_{3c}] = [X_{\theta=0^\circ} \quad X_{\theta=-120^\circ} \quad X_{\theta=120^\circ}]$
CSVPWM [22]	$X_4 = \frac{2}{\sqrt{3}}[A\sin(\omega t+\theta)] - \frac{1}{2}\{\max(X_{1a}, X_{1b}, X_{1c})\}$ $+\frac{1}{2}\{\min(X_{1a}, X_{1b}, X_{1c})\}$ $[X_{4a} \quad X_{4b} \quad X_{4c}] = [X_{\theta=0^\circ} \quad X_{\theta=-120^\circ} \quad X_{\theta=120^\circ}]$
SDPWM [23]	$X_5 = \frac{2}{\sqrt{3}}[A\sin(\omega t+\theta)] + \frac{1}{2\pi}[A\sin(3\omega t+\theta)]$ $+\frac{1}{60\pi}[A\sin(9\omega t+\theta)] + \frac{1}{120\pi}[A\sin(15\omega t+\theta)]...$ $[X_{5a} \quad X_{5b} \quad X_{5c}] = [X_{\theta=0^\circ} \quad X_{\theta=-120^\circ} \quad X_{\theta=120^\circ}]$
THISDPWM (Proposed)	$V = qB_m\sin(\omega t+\theta) + rA_m\sin(13\omega t+\theta)$ $+C\sin(\omega t+\theta)$ $V = \begin{Bmatrix} E & when\ Z \geq E \\ E & when\ Z \leq E \end{Bmatrix}$ $[V_1 \quad V_2 \quad V_3] = [V_{\theta=0^\circ} \quad V_{\theta=-120^\circ} \quad V_{\theta=120^\circ}]$

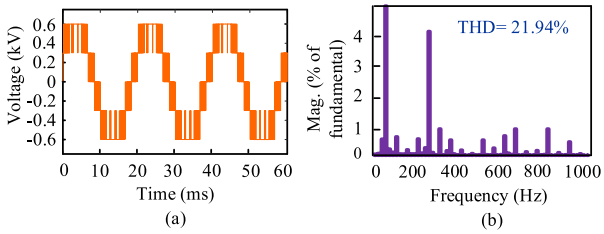

FIGURE 8. Inverter line-to-line (a) voltage waveform and (b) its frequency spectrum.

TABLE 4. Comparative study of THD against variation of modulation index.

PWM schemes	Modulation index (M_i)				
	0.7	0.8	0.9	1	1.1
THISDPWM	39.88%	35.79%	29.45%	21.94%	19.23%
SPWM [17]	44.43%	42.02%	39.49%	35.46%	32.06%
THSDPWM [18]	43.65%	40.25%	36.07%	30.94%	26.67%
CSVPWM [22]	42.39%	39.99%	33.35%	27.58%	25.91%
SDPWM [23]	43.36%	39.46%	34.68%	28.69%	25.99%
THPWM [24]	41.38%	37.67%	32.42%	26.61%	24.76%

are recorded for SPWM, THSDPWM, CSVPWM, SDPWM, and THPWM strategies, respectively. On the contrary, the proposed THISDPWM strategy shows 39.88, 21.94, and 19.23% inverter line-to-line voltage THD at Mi=0.7 (under modulation), Mi=1 (unity modulation), and Mi=1.1 (over modulation), respectively. Based on Table 4, it can be clearly viewable that the proposed THISDPWM strategy shows less inverter line-to-line voltage THD against wide range of modulation index variation compared to different existing strategies.

B. DYNAMIC RESPONSE ANALYSIS OF THE MOTOR

The dynamic behavior of IMD with the existing switching methods such as SPWM, THSDPWM, CSVPWM, SDPWM, and THPWM are depicted in Fig. 9.

Fig. 9 displays a series of waveforms, including the stator voltage (V_s), stator current (I_{abc}), speed (ω_r), and the torque (T_e), respectively. The dynamic response of IMD is obtained by varying load torque on the motor at different instant of time. Two different load torques are applied at different time span to observe the effects of load variation. The first load torque, which is 60Nm, is applied at 0.35 seconds and then removed at 0.5 seconds. The second load torque, which is 80Nm, is applied at 0.8 seconds and removed at 0.95 seconds. The dynamic response of the IMD using SPWM strategy is illustrated in Fig. 9(a). Due to inrush current flow at starting, the stator current takes 0.15s to reach its rated current. The speed also reaches its rated speed which is around 1440 r/min.

At the instant of applying torque at t=0.5s, the current started to increase and the speed is reduced which is cleared from Fig. 9(a). The THDs of stator voltage and current are found as 4.60 and 14.25% using SPWM technique.

For THSDPWM technique, the stator voltage and current THDs are obtained as 5.68 and 12.10%, respectively manifested in Fig. 9(b). A significant reduction of stator current THD can be observed for THSDPWM technique than that of the SPWM technique. However, the torque ripple is high for THSDPWM compared to SPWM. The dynamic response of the motor using CSVPWM strategy is depicted in Fig. 9(c). Significant reduction in toque ripple can be evident for dynamic response of IMD for CSVPWM technique than the existing methods. 4.9 and 8.98% THDs are recorded for stator voltage and current, respectively for the CSVPWM technique.

At the instant of employing 80Nm torque at t=0.8s, the stator current is increased and the speed is also changed. When the load is removed at t=1s, the speed settles at its previous value and the current is also decreased. The effect of load torque can be seen from the torque curve of Fig. 9(c) exhibits less amount of torque ripple than those of the SPWM and THSDPWM method, respectively. In the same way, the SDPWM presents an improved performance in terms of stator current and voltage THD than CSVPWM technique which is found as 4.45 and 7.92%, respectively as depicted in Fig. 9(d). The torque ripple is further reduced with SDPWM method due its flattening top surface. On the contrary, the stator current THD utilizing THPWM technique is found 11.34% as shown in Fig. 9(e) which is higher than those of the CSVPWM and SDPWM methods as depicted in Fig. 9(c) and Fig. 9(d), respectively. However, in terms of stator voltage THD which is recorded as 4.3%, the THPWM method outperforms than all other existing methods. Fig. 10 shows the dynamic response of the IMD with the proposed THISDPWM strategy. At t=0.18s, the motor inrush current period finishes and motor takes up its rated speed which is 1440 r/min. To observe the dynamic response of the IMD using THISDPWM strategy, 60Nm and 80Nm load torque is applied at t=0.35s and 0.8s and removed at t=0.5s and t=1s, respectively. The torque ripple is increased and stator voltage level changes slightly during this transition. However, the stator current regains its rated value and speed curve is settles at 1440 r/min when this transition ends. The stator voltage and current THDs offered by the THISDPWM technique are found 3.60 and 4.70%, respectively. The zoomed view of Fig. 10 verifies the sinusoidal nature of the stator voltage and stator current which ensures the elevated performance of the IMD with the proposed THISDPWM strategy. Additionally, the proposed THISDPWM technique reduces the torque ripple which ensures the smooth performance and increases the life expectancy of IMD. From the dynamic response of the IMD with SPWM, THSDPWM, CSVPWM, SDPWM, and THISDPWM technique it can be concluded that the proposed THISDPWM strategy offers smooth dynamic response of the motor with low stator voltage/current THD. Thus, the THISDPWM technique exhibits superior speed tracking characteristics and effectively reduces torque ripple, particularly during load variations, making it highly suitable for IMD applications.

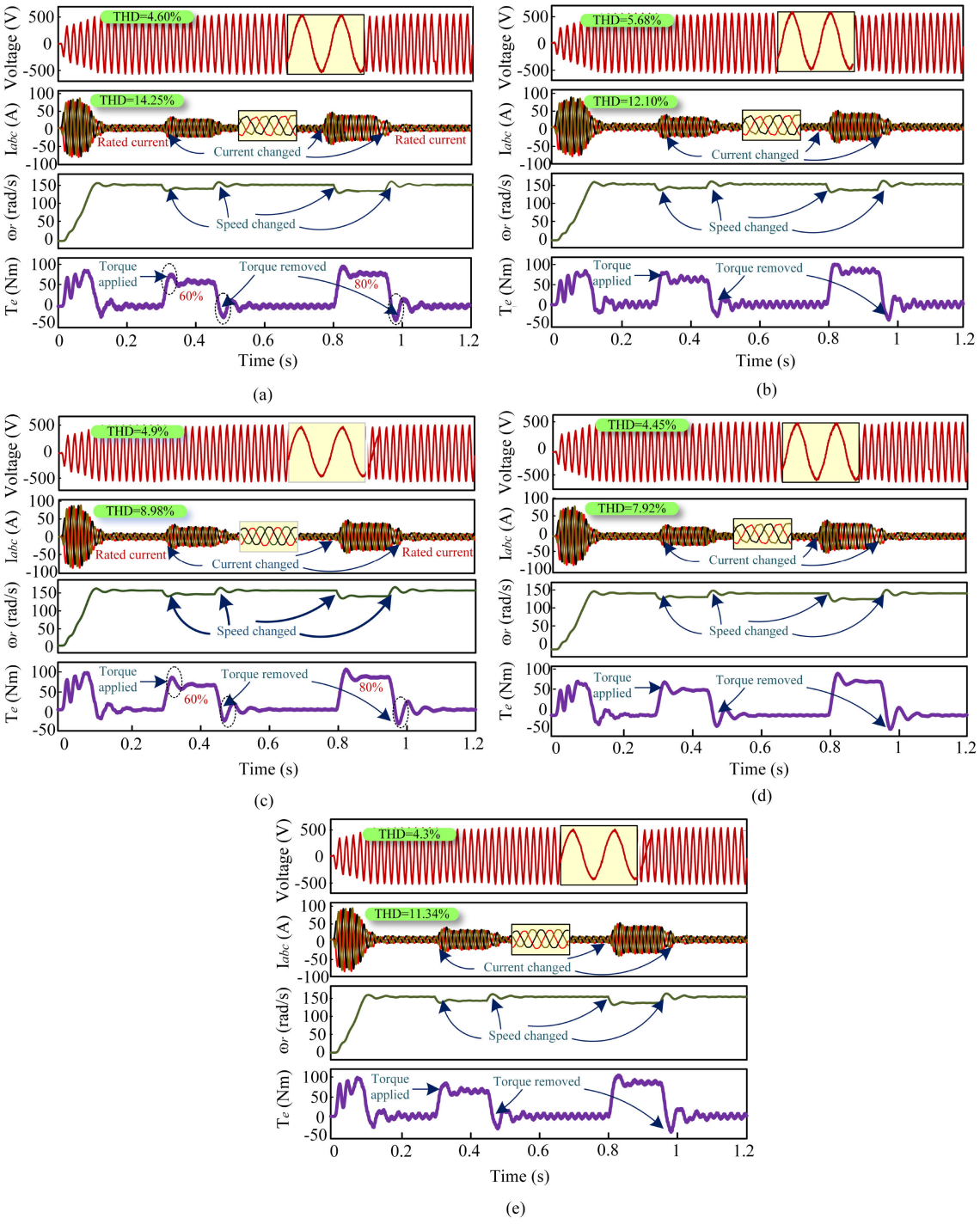

FIGURE 9. Dynamic response with different PWM strategy: (a) SPWM [17], (b)THSDPWM [18], (c) CSVPWM [22], (d)SDPWM [23], and (e) THPWM [24].

C. PV SIDE DYNAMIC RESPONSE

To validate the performance of the proposed ANN based dc-link controller, some case studies have been conducted on the output power of the PV by varying the solar insolation for the presented dc-link voltage-controlled algorithm and other existing algorithms. The dynamic response of the PV power against solar insolation variation is shown in Fig. 11. In the beginning, the solar insolation is maintained at 500 W/m^2 to monitor the state of PV power and the output dc power for different algorithms. As it can be seen from the zoomed response of Fig. 11, the proposed algorithm exhibits less oscillation while the existing P&O and InC algorithm show significant oscillation in the PV power and output dc power. The insolation is changed to 1000 W/m^2 at time t=0.25s, increasing the solar power to around 10kW. The proposed algorithm follows the MPP point in this case very smoothly

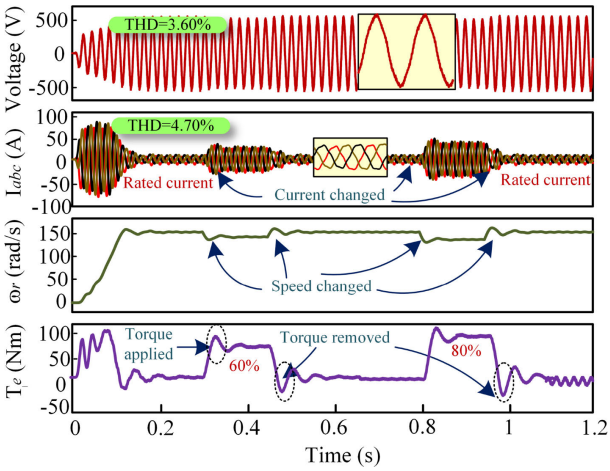

FIGURE 10. Dynamic response of the IMD using the proposed THISDPWM technique.

which verifies the primacy of the proposed algorithm. On the other hand, the P&O and InC algorithm show steady state error and takes time to settle at the desired value.

The zoomed view at the instant of changing insolation shows the tracking performance of the proposed algorithm. The proposed algorithm provides an output power of 10kW. whereas the other algorithms offer around 9.8kW output dc power. Again, at t=0.5s, the insolation is changed to 700 W/m^2 which causes the PV power and output dc power to be reduced. At the instant of changing insolation from 1000 W/m^2 to 700 W/m^2, the P&O and InC algorithm show oscillation, whereas the proposed algorithm shows smooth transition. The zoomed view shows the tracking capability of the proposed algorithm. Furthermore, the ripple at output dc power at insolation 700 W/m^2 is very low which ensures the stable dc-link voltage to enhance the performance of the drive. Consequently, when the insolation is further reduced to 300 W/m^2 at t=0.75s, the PV power and output dc power drops to 3kW.

The proposed algorithm follows the changes very rapidly while the remaining two algorithms takes time to settle at the reference value. Moreover, the P&O and InC algorithm show ripple at the output PV and dc power which is verified from the zoomed views graph segment of Fig. 11. The comparative efficiency of different MPPT tracking algorithms against PV insolation variation is depicted in Table 5. The efficiency of any algorithm can be calculated by the ratio of average power to the maximum power. The MPPT tracking efficiency is found as,

$$\eta_{pv} = \left(\frac{P_{avg}}{P_{\max}}\right) \times 100\% \tag{22}$$

where P_{avg} and P_{max} represent the average and maximum power correspondingly. For $I_r = 300$ W/m^2, the maximum power is found as 3204W. The P&O and InC algorithm result in average power output of 2853W and 3003W, respectively. Therefore, the efficiency of the P&O algorithm is calculated as 89.05%, while the efficiency of the InC algorithm is recorded as 93.75%. On the other hand, the proposed algorithm achieves an impressive efficiency of 98.93% for the same irradiation level of 300 W/m^2. The efficiency of the P&O and InC algorithms is estimated as 89.82% and 92.49%, respectively, for an irradiation of 500W/m^2. According to these findings, the InC algorithm outperforms than the P&O algorithm in terms of effectiveness.

However, the proposed algorithm still outperforms than those of the existing P&O and InC algorithms with an efficiency of 98.63%. The proposed algorithm shows an efficiency of 99.29% at 700 W/m^2 which is higher than the efficiency of the other algorithms. Finally, at 1000 W/m^2 insolation, the proposed algorithm exhibits impressive efficiency of 99.34% which makes it highly effective in tracking the MPP of the PV module across a wide range of irradiation levels.

D. RESPONSE OF PROPOSED MPPT ALGORITHM UNDER PARTIAL SHADING CONDITION

Fig. 12 illustrates the PV array characteristic curve, which serves as a means to assess the effectiveness of the proposed MPPT algorithm under different operating conditions.

Pattern 1 corresponds to a scenario characterized by uniform irradiance, wherein the global maximum power point (GMPP) is observed at 975W, as depicted in Figure 12(a). Conversely, Figure 12(b) shows the PV array response under partial shading conditions (pattern 2), revealing the presence of two local maximum power points (LMPP) at 459W and 437W alongside with one GMPP found at 588W.

Fig. 13 exhibits the response of the PV system under both uniform and partial shading conditions, utilizing the proposed MPPT algorithm. Initially, the PV array is commenced with uniform solar insolation (1000W/m^2) and temperature (25°C), according to pattern 1 which is shown in Fig. 12(a). From the P-V and I-V curve, it is clear that the proposed MPPT algorithm quickly tracks GMPP at 975W. At t=5.5s, the PV system is transitioned to partial shading from constant insolation condition to evaluate the performance of MPPT algorithm. Two panels are exposed to 1000W/m^2 of insolation while the remaining ones are partially shaded and exposed to 750W/m^2 and 400W/m^2, respectively. When confronted with pattern 2, the proposed MPPT algorithm tries to track GMPP, resulting in oscillatory behavior around the MPP, as evident from Fig. 13.

E. DYNAMIC RESPONSE OF IMD DURING STEP CHANGE IN SOLAR INSOLATION

Dynamic response of the IMD due to the step change in solar insolation utilizing the proposed MPPT algorithm and THISDPWM technique is depicted in Fig. 14. The insolation decreases from 1000W/m^2 to 500W/m^2 at 0.8s. From the P-V and I-V curve, it can be verified that there is no significant change in the voltage at maximum power (V_{PV}). However, the current at the MPP (I_{PV}) exhibits a drastic change, reflecting the sensitivity of the IMD to variation in insolation level. The dc-link voltage (V_{dc}) remains normal during the step

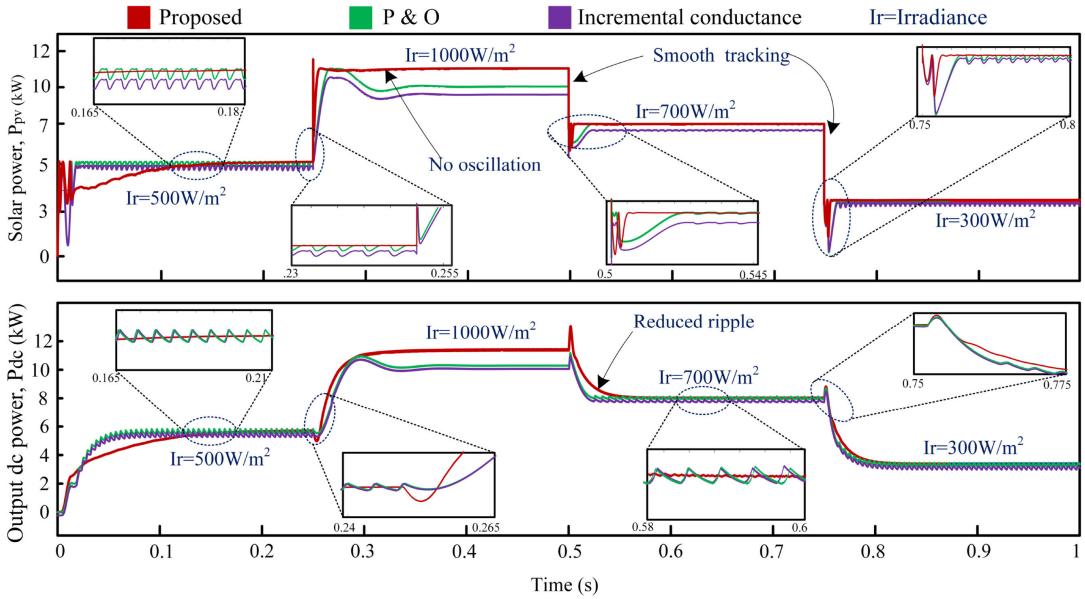

FIGURE 11. Dynamic response of output PV and dc power for different MPPT algorithms with the change of PV insolation.

TABLE 5. Comparison of efficiency among different MPPT algorithms.

S.N.	Irradiation (W/m^2)	P_{max} (W)	P&O Algorithm		Incremental Conductance		Proposed Algorithm	
			P_{avg} (W)	η (%)	P_{avg} (W)	η (%)	P_{avg} (W)	η (%)
01.	300	3204	2853	89.05%	3003	93.75%	3170	98.93%
02.	500	5395	4774	88.99%	5146	95.39%	5370	99.53%
03.	700	7563	6820	90.17%	7238	95.71%	7540	99.69%
04.	1000	10760	9705	90.20%	10384	96.51%	10740	99.81%

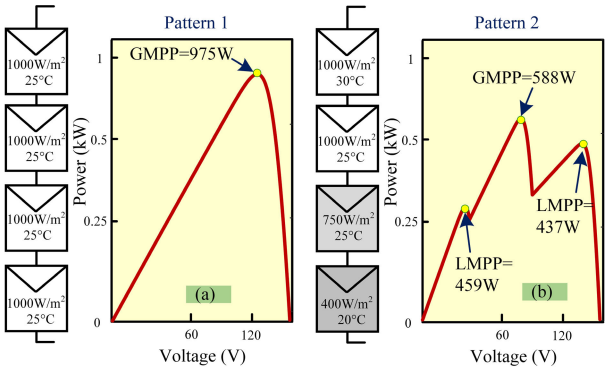

FIGURE 12. PV array characteristic curve for evaluating the performance of proposed MPPT algorithm: (a) uniform irradiance condition (pattern 1) and (b) partial shading condition (pattern 2).

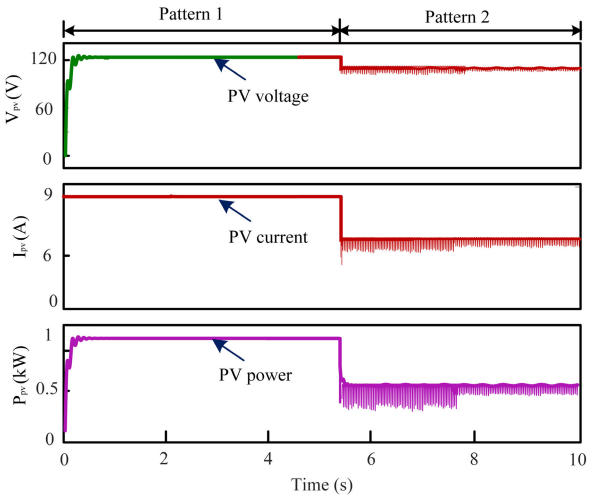

FIGURE 13. PV array response under uniform and partial shading condition.

change. Once the MPPT algorithm successfully tracks the MPP, it effectively maintains the operating point at that MPP. This demonstrates the effectiveness of the proposed algorithm in optimizing the performance of the IMD under varying insolation conditions. Fig. 14 also shows the stator current (I_{abc}), speed (ω_r), and torque (T_e) curve for the step change in solar insolation. At t=0.8 seconds, the stator current decreases due to the reduction in power caused by the decrease in insolation. Additionally, the speed settles at a lower value of around 142 rad/s, indicating the response of the IMD to the changed operating conditions.

TABLE 6. Comparison of power losses among different PWM strategies.

PWM techniques	Losses (% of input power)	Modulation index (M_i)				
		0.6	0.7	0.8	0.9	1
THISDPWM	Conduction loss, P_{CL}	0.512	0.478	0.429	0.388	0.337
	Switching loss, P_{SL}	0.302	0.291	0.281	0.241	0.235
	Total loss, P_{TOT}	0.814	0.769	0.71	0.629	0.572
SPWM [17]	Conduction loss, P_{CL}	0.529	0.496	0.416	0.398	0.348
	Switching loss, P_{SL}	0.369	0.316	0.297	0.298	0.256
	Total loss, P_{TOT}	0.898	0.812	0.713	0.696	0.604
THSDPWM [18]	Conduction loss, P_{CL}	0.556	0.516	0.496	0.453	0.436
	Switching loss, P_{SL}	0.355	0.317	0.295	0.259	0.236
	Total loss, P_{TOT}	0.911	0.833	0.791	0.712	0.672
CSVPWM [22]	Conduction loss, P_{CL}	0.501	0.486	0.441	0.399	0.369
	Switching loss, P_{SL}	0.319	0.293	0.274	0.258	0.231
	Total loss, P_{TOT}	0.82	0.779	0.715	0.657	0.6
SDPWM [23]	Conduction loss, P_{CL}	0.513	0.499	0.423	0.412	0.401
	Switching loss, P_{SL}	0.383	0.327	0.311	0.277	0.237
	Total loss, P_{TOT}	0.896	0.826	0.734	0.689	0.638
THPWM [24]	Conduction loss, P_{CL}	0.537	0.499	0.423	0.401	0.357
	Switching loss, P_{SL}	0.355	0.327	0.311	0.296	0.267
	Total loss, P_{TOT}	0.892	0.826	0.734	0.697	0.624

F. DYNAMIC RESPONSE OF IMD DURING GRADUAL DECREASE IN SOLAR INSOLATION

Fig. 15 represents the response of the solar PV array and IMD during a gradual transition of insolation levels from 1000W/m^2 to 500W/m^2 and back to 1000W/m^2. the voltage at maximum power (V_{PV}) is effectively regulated by the proposed MPPT algorithm throughout the slow decline in insolation, ensuring its consistency. However, during the subsequent increase in insolation, V_{PV} exhibits a slight increase, as observed from the P-V and I-V curves. In contrast, the dc-link voltage (V_{dc}) remains stable despite the fluctuations in insolation levels. Moreover, the current at the MPP (I_{PV}) displays significant variations in accordance with changes in insolation. Additionally, Fig. 15 shows that the IMD operates consistently at its rated current, irrespective of changes in insolation. Notably, the speed curve closely tracks the reference speed of 150 rad/s, emphasizing the robust performance of the IMD using the proposed THISDPWM technique.

G. INSPECTION OF POWER LOSS

Conduction losses and switching losses are the two categories into which the power losses in a converter can be divided. When the power switches/IGBTs are in on state, the voltage drops across the switches and the current flowing through them serve as indicator of conduction losses (P_{CLoss}). The average conduction loss of a single IGBT is given by,

$$P_{CLoss} = \frac{1}{2\pi}\left[\int_0^{2\pi} [v_{ce}(t)\ i_c(t)]\ d\,(wt) + \int_0^{2\pi} [v_F(t)\, i_F(t)]\ d(wt)\right] \tag{23}$$

where, $v_{ce}(t)$, $v_F(t)$, $i_c(t)$, and $i_F(t)$ represent the instantaneous voltage across the switch, the instantaneous voltage across the body diode, the instantaneous current through the switch, and the instantaneous current through the body diode, respectively. The switching losses (P_{SLoss}) occur during the turn-on and turn-off period of the power devices. The total switching losses can be represented as,

$$P_{SLoss} = \frac{1}{T_o}\left[\sum_{i=1}^{N} E_{on_i}(i_c) + \sum_{i=1}^{N} E_{off_i}(i_c) + \sum_{i=1}^{N} E_{rec_i}(i_F)\right] \tag{24}$$

where, E_{on}, E_{off}, and E_{rec} indicate the switch turn-on loss, turn-off loss and diode turn-off loss in joule, respectively.

The power losses of the 3-level NPC inverter are computed using an industrially available IGBT module IKW40N65F5 from Infineon Technologies. Table 6 shows the comparison of power losses among different PWM methods against the variation of modulation index.

From Table 6, it can be seen that for $M_i = 0.6$, the total loss using THSDPWM is the loftiest among all the switching techniques whereas the THISDPWM technique shows a power loss of 0.814% which validates the improved performance of the proposed PWM method even in under modulation region. It is also evident from Table 6 that the proposed THISDWPM method exhibits 8.67% conduction loss and 8.2% switching loss as compared to the SPWM method. Fig 16 shows the graphical total losses of different PWM techniques with respect to modulation index. During loss analysis, switching frequency is considered as 5kHz.

The proposed THISDPWM technique offers total loss of 0.572% whereas the SPWM, THSDPWM, CSVPWM,

TABLE 7. Comparative performance analysis among different PWM schemes.

S.N.	PWM technique	Modulation index, m_i	THD (%)		Torque ripple (Nm)	DC link voltage (V)
			V_s	I_s		
01.	SPWM [11]	1	4.6	14.25	7.34	650
02.	THSDPWM [12]	1	5.68	12.10	13.45	650
03.	CSVPWM [16]	1	4.9	8.98	8.11	650
04.	SDPWM [17]	1	4.45	7.92	12.34	650
05.	THPWM [18]	1	4.3	11.34	11.55	650
06.	THISDPWM	1	3.60	4.70	5.21	650

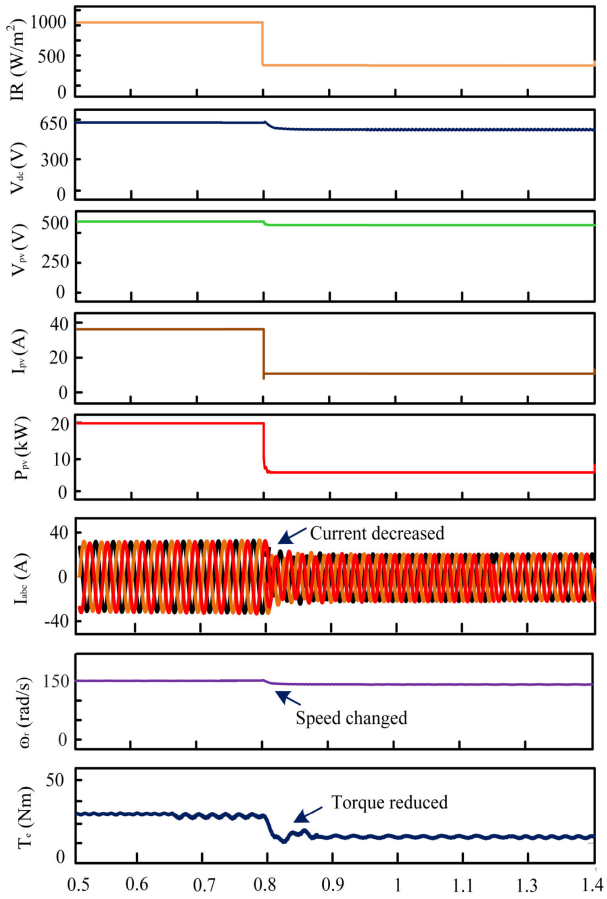

FIGURE 14. Solar PV array and IMD responses during step change in insolation from 1000W/m^2 to 500W/m^2.

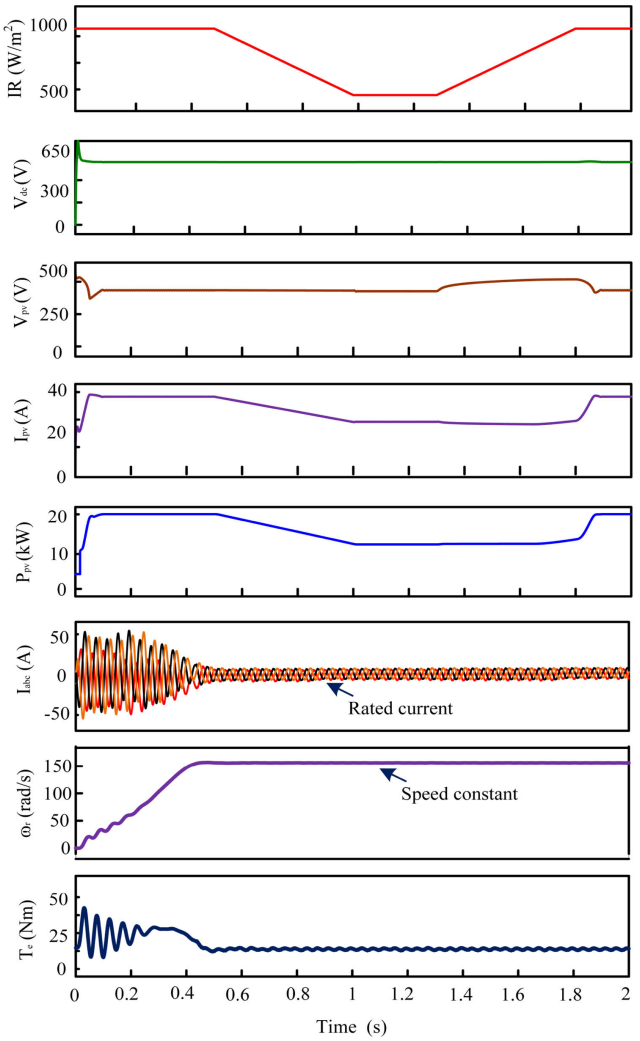

FIGURE 15. Solar PV array and IMD responses during gradual decrease in insolation from 1000W/m^2 to 500W/m^2.

SDPWM, and THPWM offers 0.604,0.672, 0.6, 0.638, and 0.624%, respectively. From Table 6 and Fig. 16, it is clearly notable that the proposed THISDPWM technique shows better performance in terms of power loss compared to other PWM strategies.

V. COMPARATIVE RESULTS ANALYIS

In Table 7, comparative study among various PWM methods in terms of stator voltage THD, stator current THD, and torque ripple of the motor is shown. The modulation index and dc-link voltage are set to 1 and 650V while preparing Table 7. The existing SPWM, THSDPWM, CSVPWM,

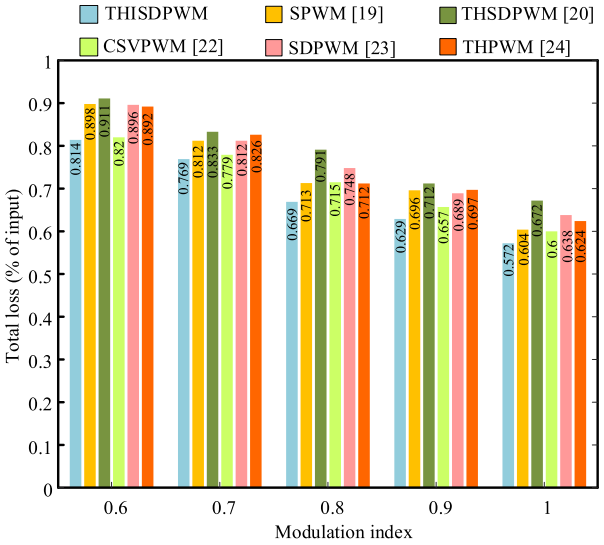

FIGURE 16. Comparison of total power loss with respect to variation of modulation index.

FIGURE 17. Photograph of the experimental setup.

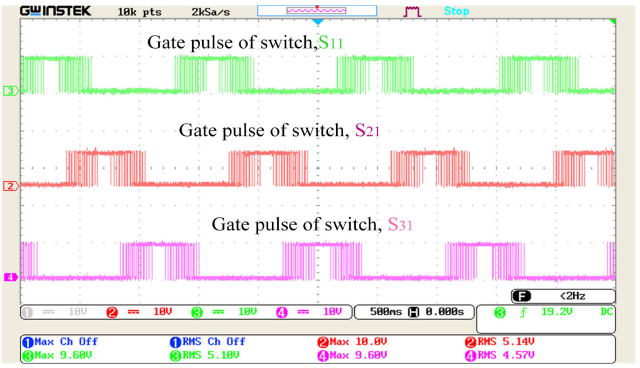

FIGURE 18. Experimental gate pulses with the proposed THISDPWM strategy.

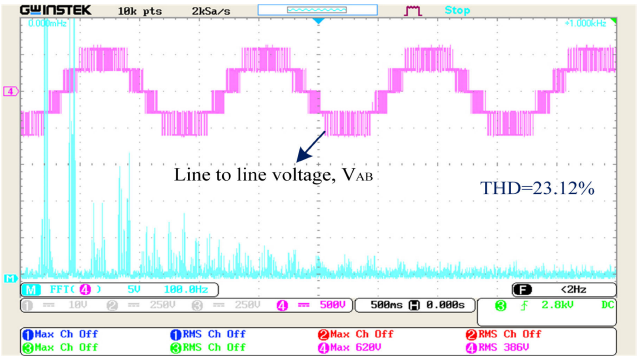

FIGURE 19. Inverter output line-to-line voltage and its frequency spectra with the proposed THISDPWM strategy.

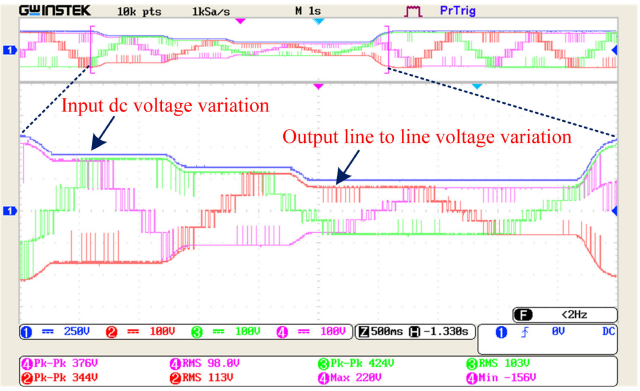

FIGURE 20. Dynamic response of the inverter line-to-line voltage with the variation of dc-link voltage.

SDPWM, and THPWM methods show the filtered stator voltage THD of 4.6, 5.68, 4.9, 4.45, and 4.3%, respectively. On the other hand, THISDPWM technique offers 3.60% filtered stator voltage THD which ensures the smooth operation of IMD by reducing the harmonics significantly as compared to other methods. Torque ripple is one of the main concern of IMD which is a measure of smooth or vibrationless operation of the motor. The SPWM and CSVPWM technique produces 7.34Nm and 8.11Nm torque vibration which are lowest among the existing methods. Whereas the proposed THISDPWM strategy offers 4.70Nm torque ripple which ensures smooth and reduced vibration operation of the motor as compared to other methods. Moreover, the existing SPWM, THSDPWM, CSVPWM, SVPWM, and THPWM methods show 14.25, 12.10, 8.98, 7.92, and 11.34% stator current THD which do not follow the IEEE-519 power quality standard. Whereas the proposed THISDPWM offers 4.70% stator current THD which meet the power quality standard of IEEE-519. Finally, it can be concluded that the proposed THISDPWM strategy show promising performance in term of stator voltage/current THD and torque ripple of the motor compared to existing counterparts.

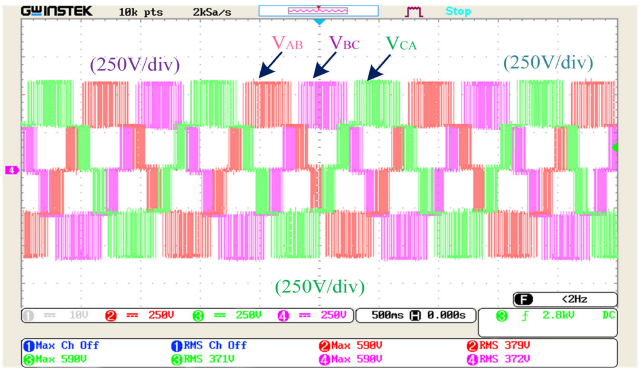

FIGURE 21. Unfiltered inverter line-to-line voltage waveform.

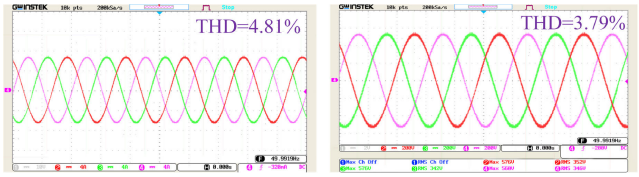

FIGURE 22. Experimental waveforms of (a) stator current and (b) stator voltage.

VI. EXPERIMENTAL VALIDATION

An experiment is conducted on a 2.2 kW squirrel cage IM with the specifications listed in the Appendix and its prototype shown in Fig. 17 to verify the simulation. The 3-level NPC inverter and the dc-dc converter are constructed using IKW40N65F5 IGBTs from Infineon Technologies.

The IGBT has an internal anti-parallel body diode that blocks the flow of reverse current. 2.5 kW solar PV array is utilized here to drive the 2.2kW IM. As the system control board, a TMS320F28335 DSP processor chip is utilized. The custom gate driver circuit, which makes use of TLP 250 optocouplers and B1212S-1W isolated dc-dc converters, boosts the gate pulses from the DSP board for the specified IGBTs. Between the high voltage gate side circuit of the IGBT and the low voltage logic level circuit of the DSP board, optocouplers are used to maintain separation. Through a lab bench power source, a 15V dc supply is used to power the gate drivers of the IGBTs. The findings of the experiment are recorded though a 4-channel oscilloscope (GDS-1104B). The generated experimental gate pulses with the proposed THISDPWM method are shown in Fig. 18.

From Fig. 18, the generated gate pulses are balanced and symmetric. The experimental unfiltered inverter line-to-line voltage waveform is shown in Fig. 19 with 23.12% THD. To observe the dynamic behavior of the inverter, a dc-link variation test is conducted. The dynamic inverter output voltage against dc-link voltage variation is shown in Fig. 20. In Fig. 21, the 3-phase unfiltered inverter line-to-line voltage is shown. The experimental stator current and stator voltage are shown in Fig. 22 with 4.81% and 3.79% THD, respectively. Thus, the experimental findings

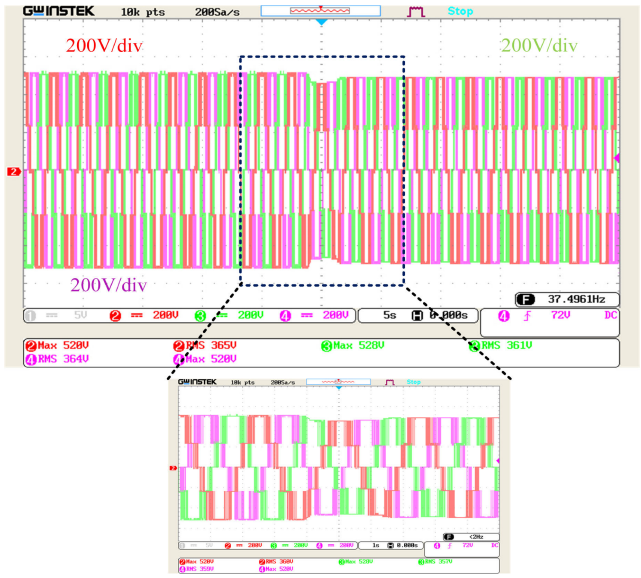

FIGURE 23. Dynamic response of the stator voltage with the step change in solar insolation.

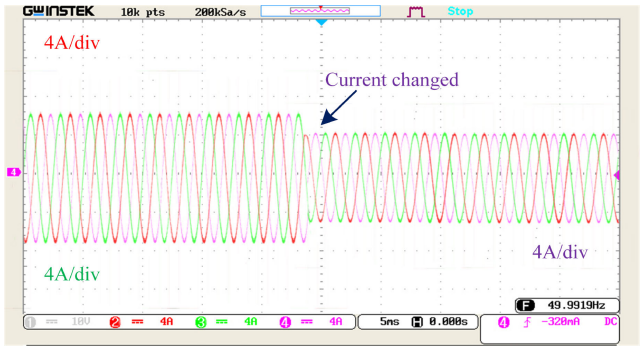

FIGURE 24. Dynamic response of the stator current with the step change in solar insolation.

validate the desired performances of the proposed PWM strategy.

Fig. 23 and 24 present the experimental results of the stator voltage and current response to a change in insolation level from 1000W/m^2 to 500W/m^2. During the transition, it is observed that the stator voltage experiences a slight reduction at the moment of changing insolation. However, it quickly recovers and returns to its previous value. This behavior suggests a transient response of the stator voltage to the alteration in insolation levels. Conversely, the stator current exhibits a noticeable decrease and eventually settles at a new value. This change in current can be observed from Fig. 24.

VII. CONCLUSION

In this work, a modified PWM strategy and an ANN based improved MPPT algorithm are proposed to improve the performance of a solar PV fed 3-level NPC inverter driven IMD. The ANN based InC MPPT algorithm shows higher efficiency with stable dc-link voltage against different PV

parameters variation. 99.34% MPPT tracking efficiency is achieved with the proposed algorithm at 1000W/m^2 solar insolation. In addition, the proposed THISDPWM strategy improves the THD of stator voltage and current, power loss, and torque ripple of the motor compared to existing SPWM, THSDPWM, CSVPWM, SVPWM, and THPWM methods. The proposed THISDPWM strategy shows 3.60% and 4.70% THDs for stator voltage and current respectively which meet the power quality standard of IEEE-519 standard at filtered condition. On the contrary, 21.94% unfiltered inverter output voltage is recorded for the proposed THISDPWM strategy which is also lower than those of the existing methods. Thus, the proposed THISDPWM strategy reduce the filter size. The total power loss and torque ripple are also low for the proposed THISDPWM strategy compared to existing counterparts. Thus, the proposed ANN based MPPT algorithm and the PWM strategy could be consider as the best choices for other multilevel inverter-based power system applications.

APPENDIX

Induction motor specifications: 2.2kW (3 hp), 3-phase, 400 V, 4 poles, $R_s = 0.623\Omega$, $L_{ls} = 0.00243$H, $R_r = 0.65\Omega$, $L_{lr} = 0.00243$H, $L_m = 0.07203$H, $J = 0.012$Kg-m^2

ACKNOWLEDGMENT

Author Contributions: Nazmul Islam Nahin and Shuvra Prokash Biswas conceived the main idea; Sudipto Mondal designed the experiments and ensured the hardware validation. Md. Rabiul Islam and S. M. Muyeen analyzed the data; Nazmul Islam Nahin, Shuvra Prokash Biswas, and Sudipto Mondal collected and processed the data; Md. Rabiul Islam and S. M. Muyeen interpreted the results and drew the conclusions; and Nazmul Islam Nahin and Shuvra Prokash Biswas wrote the article.

REFERENCES

[1] M. R. Islam, A. M. Mahfuz-Ur-Rahman, K. M. Muttaqi, and D. Sutanto, "State-of-the-art of the medium-voltage power converter technologies for grid integration of solar photovoltaic power plants," *IEEE Trans. Energy Convers.*, vol. 34, no. 1, pp. 372–384, Mar. 2019.

[2] X. Li, H. Wen, Y. Hu, Y. Du, and Y. Yang, "A comparative study on photovoltaic MPPT algorithms under EN50530 dynamic test procedure," *IEEE Trans. Power Electron.*, vol. 36, no. 4, pp. 4153–4168, Apr. 2021.

[3] A. A. S. Mohamed, A. Berzoy, and O. A. Mohammed, "Design and hardware implementation of FL-MPPT control of PV systems based on GA and small-signal analysis," *IEEE Trans. Sustain. Energy*, vol. 8, no. 1, pp. 279–290, Jan. 2017.

[4] I. Pervez, I. Shams, S. Mekhilef, A. Sarwar, M. Tariq, and B. Alamri, "Most valuable player algorithm based maximum power point tracking for a partially shaded PV generation system," *IEEE Trans. Sustain. Energy*, vol. 12, no. 4, pp. 1876–1890, Oct. 2021.

[5] V. R. Kota and M. N. Bhukya, "A novel linear tangents based P&O scheme for MPPT of a PV system," *Renew. Sustain. Energy Rev.*, vol. 71, pp. 257–267, May 2017.

[6] J. Ahmed and Z. Salam, "An enhanced adaptive P&O MPPT for fast and efficient tracking under varying environmental conditions," *IEEE Trans. Sustain. Energy*, vol. 9, no. 3, pp. 1487–1496, Jul. 2018.

[7] M. Lasheen and M. Abdel-Salam, "Maximum power point tracking using Hill climbing and ANFIS techniques for PV applications: A review and a novel hybrid approach," *Energy Convers. Manage.*, vol. 171, pp. 1002–1019, Sep. 2018.

[8] S. Allahabadi, H. Iman-Eini, and S. Farhangi, "Fast artificial neural network based method for estimation of the global maximum power point in photovoltaic systems," *IEEE Trans. Ind. Electron.*, vol. 69, no. 6, pp. 5879–5888, Jun. 2022.

[9] S. R. Kiran, C. H. H. Basha, V. P. Singh, C. Dhanamjayulu, B. R. Prusty, and B. Khan, "Reduced simulative performance analysis of variable step size ANN based MPPT techniques for partially shaded solar PV systems," *IEEE Access*, vol. 10, pp. 48875–48889, 2022.

[10] A. F. Mirza, M. Mansoor, Q. Ling, M. I. Khan, and O. M. Aldossary, "Advanced variable step size incremental conductance MPPT for a standalone PV system utilizing a GA-tuned PID controller," *Energies*, vol. 13, no. 16, p. 4153, Aug. 2020.

[11] C. R. N. Algar, J. T. Giraldo, and O. R. Alvarez, "Fuzzy logic based MPPT controller for a PV system," *Energies*, vol. 10, no. 12, p. 2036, Dec. 2017.

[12] R. Kumar, P. Kant, and B. Singh, "Harmonic suppression scheme for multipulse converter fed multilevel inverter-based IM drive," *IEEE Trans. Ind. Appl.*, vol. 57, no. 6, pp. 6058–6068, Nov. 2021.

[13] S. P. Biswas, S. Haq, M. R. Islam, M. K. Hosain, and R. N. Shaw, "Advanced level shifted carrier based bus clamping PWM technique for a 54 pulse AC to DC converter fed MLI based induction motor drive," in *Proc. IEEE 6th Int. Conf. Comput., Commun. Autom. (ICCCA)*, Arad, Romania, Dec. 2021, pp. 587–592.

[14] H. Mhiesan, Y. Wei, Y. P. Siwakoti, and H. A. Mantooth, "A fault-tolerant hybrid cascaded H-bridge multilevel inverter," *IEEE Trans. Power Electron.*, vol. 35, no. 12, pp. 12702–12715, Dec. 2020.

[15] S. Haq, S. P. Biswas, M. K. Hosain, M. R. Islam, M. A. Rahman, and K. M. Muttaqi, "A modified PWM scheme to improve the power quality of NPC inverter based solar PV fed induction motor drive for water pumping," in *Proc. IEEE Ind. Appl. Soc. Annu. Meeting (IAS)*, Vancouver, BC, Canada, Oct. 2021, pp. 1–6.

[16] A. M. Mahfuz-Ur-Rahman, M. R. Islam, K. M. Muttaqi, and D. Sutanto, "A magnetic-linked multilevel active neutral point clamped converter with an advanced switching technique for grid integration of solar photovoltaic systems," *IEEE Trans. Ind. Appl.*, vol. 56, no. 2, pp. 1990–2000, Mar. 2020.

[17] N. Sandeep and U. R. Yaragatti, "A switched-capacitor-based multilevel inverter topology with reduced components," *IEEE Trans. Power Electron.*, vol. 33, no. 7, pp. 5538–5542, Jul. 2018.

[18] S. Haq, S. P. Biswas, M. K. Hosain, M. A. Rahman, M. R. Islam, R. M. Elavarasan, and K. M. Muttaqi, "A modified PWM scheme to improve the power quality of NPC inverter based solar PV fed induction motor drive for water pumping," *IEEE Trans. Ind. Appl.*, vol. 59, no. 3, pp. 3019–3030, May/Jun. 2023, doi: 10.1109/TIA.2023.3245590.

[19] S. Haq, S. P. Biswas, and M. K. Hosain, "Performance investigation of different modulation schemes for an 11-level NPC inverter fed induction motor drive," in *Proc. Int. Conf. Autom., Control Mechatronics Ind. 4.0 (ACMI)*, Rajshahi, Bangladesh, Jul. 2021, pp. 1–6.

[20] F. Deng and Z. Chen, "Voltage-balancing method for modular multilevel converters under phase-shifted carrier-based pulsewidth modulation," *IEEE Trans. Ind. Electron.*, vol. 62, no. 7, pp. 4158–4169, Jul. 2015.

[21] S. P. Biswas, M. S. Anower, S. Haq, M. R. Islam, M. A. Rahman, and K. M. Muttaqi, "A new level shifted carrier based PWM technique for a 5-level multilevel inverter used in induction motor drives," in *Proc. IEEE Ind. Appl. Soc. Annu. Meeting (IAS)*, Vancouver, BC, Canada, Oct. 2021, pp. 1–6.

[22] P. Chudzik, M. Steczek, and K. Tatar, "Reduction in selected torque harmonics in a three-level NPC inverter-fed induction motor drive," *Energies*, vol. 15, no. 11, p. 4078, Jun. 2022, doi: 10.3390/en15114078.

[23] S. P. Biswas, M. S. Anower, M. R. I. Sheikh, M. R. Islam, and K. M. Muttaqi, "Investigation of the impact of different PWM techniques on rectifier-inverter fed induction motor drive," in *Proc. Australas. Univ. Power Eng. Conf. (AUPEC)*, Hobart, TAS, Australia, Nov. 2020, pp. 1–6.

[24] C. Ramulu, P. Sanjeevikumar, R. Karampuri, S. Jain, A. H. Ertas, and V. Fedak, "A solar PV water pumping solution using a three-level cascaded inverter connected induction motor drive," *Eng. Sci. Technol., Int. J.*, vol. 19, no. 4, pp. 1731–1741, Dec. 2016.

[25] S. S. Lee, M. Sidorov, N. R. N. Idris, and Y. E. Heng, "A symmetrical cascaded compact-module multilevel inverter (CCM-MLI) with pulsewidth modulation," *IEEE Trans. Ind. Electron.*, vol. 65, no. 6, pp. 4631–4639, Jun. 2018.

[26] S. Shila, S. P. Biswas, M. R. Islam, M. M. Rahman, G. Shafiullah, and O. A. Sadaba, "A new PWM scheme to improve the input power quality of 18-pulse rectifier fed 3-level NPC inverter based induction motor drive," in *Proc. 31st Australas. Univ. Power Eng. Conf. (AUPEC)*, Perth, WA, Australia, Sep. 2021, pp. 1–6.
[27] S. Albatran, A. S. Allabadi, A. R. A. Khalaileh, and Y. Fu, "Improving the performance of a two-level voltage source inverter in the overmodulation region using adaptive optimal third harmonic injection pulsewidth modulation schemes," *IEEE Trans. Power Electron.*, vol. 36, no. 1, pp. 1092–1103, Jan. 2021.
[28] S. Shukla and B. Singh, "Single-stage PV-grid interactive induction motor drive with improved flux estimation technique for water pumping with reduced sensors," *IEEE Trans. Power Electron.*, vol. 35, no. 12, pp. 12988–12999, Dec. 2020.

NAZMUL ISLAM NAHIN was born in Cox's Bazar, Chattogram, Bangladesh, in 2000. He is currently pursuing the B.Sc. degree in electronics and telecommunication engineering (ETE) with the Faculty of Electrical and Computer Engineering, Rajshahi University of Engineering and Technology (RUET), Rajshahi, Bangladesh. His research interests include power electronics, power quality, electrical machines and drives, renewable energy systems, and smart micro-grids. He received the Best Paper Award at ICEEE 2022 and ICECE 2022.

SHUVRA PROKASH BISWAS (Student Member, IEEE) received the B.Sc. degree in electronics and telecommunication engineering (ETE) and the M.Sc. degree in electrical and electronic engineering (EEE) from the Rajshahi University of Engineering and Technology (RUET), Rajshahi, Bangladesh, in 2017 and 2021, respectively.

He has been working as an Assistant Professor with the Department of ETE, RUET, since December 2021. He has authored and coauthored more than 50 technical articles and two book chapters. His research interests include power electronics, electrical machines and drives, power quality, renewable energy systems, artificial intelligence, machine learning, real-time hardware-in-the-loop (HIL) simulations, and smart micro-grids. He received the Best Paper Award at ICECTE 2019, IEEE ASEMD 2020, IEEE IAS GUCON 2021, IEEE IAS ICCCA 2021, ICEEE 2022, and ICECE 2022. He has served as a Reviewer for IEEE Transactions on Industrial Electronics, IEEE Transactions on Energy Conversion, IEEE Transactions on Industry Applications, IEEE Transactions on Circuits and Systems—II: Express Briefs, IEEE Transactions on Applied Superconductivity, IEEE Systems Journal, and IEEE Access.

SUDIPTO MONDAL was born in Rajbari, Dhaka, Bangladesh, in 2002. He is currently pursuing the B.Sc. degree in electronics and telecommunication engineering (ETE) with the Faculty of Electrical and Computer Engineering, Rajshahi University of Engineering and Technology (RUET), Rajshahi, Bangladesh.

His current research interests include power electronics, power quality, electrical machines and drives, grid integration of renewable energy sources, and smart micro-grids. He received the Best Paper Award at ICECE 2022.

MD. RABIUL ISLAM (Senior Member, IEEE) received the Ph.D. degree in electrical engineering from the University of Technology Sydney (UTS), Sydney, Australia, in 2014.

He is currently a Senior Lecturer with the School of Electrical, Computer, and Telecommunications Engineering (SECTE), University of Wollongong (UOW), NSW, Australia. He has authored or coauthored more than 350 papers, including more than 100 IEEE Transactions/IEEE journal articles. He has written or edited seven technical books published by Springer and Taylor & Francis. His research interests include power electronic converters, renewable energy technologies, power quality, electrical machines, electric vehicles, and smart grid. He has received several Best Paper Awards including two Best Paper recognitions from IEEE Transactions on Energy Conversion, in 2020. He is serving as an Associate Editor for the IEEE Transactions on Industrial Electronics, IEEE Transactions on Energy Conversion, IEEE Power Engineering Letters, and IEEE Access. As a Lead Guest Editor, he has organized the first joint IEEE Industrial Electronics Society and the IEEE Power and Energy Society Special Section entitled Advances in High-Frequency Isolated Power Converters. He is an Editor of the Book Series titled *Advanced Power Electronics Converters* (CRC Press, Taylor & Francis Group). He has received several funding from government and industries, including in total U.S. $5.48 million from the Australian Government through the Australian Research Council (ARC) Discovery Project (DP) 2020 entitled A Next Generation Smart Solid-State Transformer for Power Grid Applications and the ARC Industrial Transformation Training Centre Project 2021 entitled ARC Training Centre in Energy Technologies for Future Grids.

S. M. MUYEEN (Senior Member, IEEE) received the B.Sc.Eng. degree in electrical and electronic engineering from the Rajshahi University of Engineering and Technology (RUET, formerly known as the Rajshahi Institute of Technology), Bangladesh, in 2000, and the M.Eng. and Ph.D. degrees in electrical and electronic engineering from the Kitami Institute of Technology, Japan, in 2005 and 2008, respectively. Currently, he is a Full Professor with Electrical Engineering Department, Qatar University. He has been a keynote speaker and an invited speaker at many international conferences, workshops, and universities. He has published more than 250 papers in different journals and international conferences. He has published seven books as the author or an editor. His research interests include power system stability and control, electrical machine, FACTS, energy storage systems (ESSs), renewable energy, and HVdc systems. He is a fellow of Engineers Australia. He is serving as an Editor/Associate Editor for many prestigious journals from IEEE, IET, and other publishers, including IEEE Transactions on Energy Conversion, IEEE Power Engineering Letters, *IET Renewable Power Generation*, and *IET Generation, Transmission and Distribution*.